COS-derived GPP relationships with temperature and light help explain high-latitude atmospheric CO_2 seasonal cycle amplification

Lei Hu[a,b,1], Stephen A. Montzka[b], Aleya Kaushik[a,b], Arlyn E. Andrews[b], Colm Sweeney[b], John Miller[b], Ian T. Baker[c], Scott Denning[c], Elliott Campbell[d], Yoichi P. Shiga[e], Pieter Tans[b], M. Carolina Siso[a,b], Molly Crotwell[a,b], Kathryn McKain[a,b], Kirk Thoning[b], Bradley Hall[b], Isaac Vimont[a,b], James W. Elkins[b], Mary E. Whelan[f], and Parvadha Suntharalingam[g]

[a]Cooperative Institute for Research in Environmental Sciences, University of Colorado Boulder, Boulder, CO 80309; [b]Global Monitoring Laboratory, National Oceanic and Atmospheric Administration, Boulder, CO 80305; [c]Department of Atmospheric Science, Colorado State University, Fort Collins, CO 80523; [d]Environmental Studies Department, University of California, Santa Cruz, CA 95064; [e]Earth Science, Universities Space Research Association, Mountain View, CA 94043; [f]Department of Environmental Sciences, Rutgers University, New Brunswick, NJ 08901; and [g]School of Environmental Sciences, University of East Anglia, Norwich NR4 7TJ, United Kingdom

Edited by Almut Arneth, Karlsruher Institut für Technologie, Garmisch-Partenkirchen, Germany, and accepted by Editorial Board Member Akkihebbal R. Ravishankara June 27, 2021 (received for review February 19, 2021)

In the Arctic and Boreal region (ABR) where warming is especially pronounced, the increase of gross primary production (GPP) has been suggested as an important driver for the increase of the atmospheric CO_2 seasonal cycle amplitude (SCA). However, the role of GPP relative to changes in ecosystem respiration (ER) remains unclear, largely due to our inability to quantify these gross fluxes on regional scales. Here, we use atmospheric carbonyl sulfide (COS) measurements to provide observation-based estimates of GPP over the North American ABR. Our annual GPP estimate is 3.6 (2.4 to 5.5) PgC · y^{-1} between 2009 and 2013, the uncertainty of which is smaller than the range of GPP estimated from terrestrial ecosystem models (1.5 to 9.8 PgC · y^{-1}). Our COS-derived monthly GPP shows significant correlations in space and time with satellite-based GPP proxies, solar-induced chlorophyll fluorescence, and near-infrared reflectance of vegetation. Furthermore, the derived monthly GPP displays two different linear relationships with soil temperature in spring versus autumn, whereas the relationship between monthly ER and soil temperature is best described by a single quadratic relationship throughout the year. In spring to midsummer, when GPP is most strongly correlated with soil temperature, our results suggest the warming-induced increases of GPP likely exceeded the increases of ER over the past four decades. In autumn, however, increases of ER were likely greater than GPP due to light limitations on GPP, thereby enhancing autumn net carbon emissions. Both effects have likely contributed to the atmospheric CO_2 SCA amplification observed in the ABR.

carbonyl sulfide | gross primary production | Arctic and Boreal ecosystems | CO_2 seasonal cycle amplitude | climate change

Gross primary production (GPP) is the total amount of carbon that is taken up from the atmosphere and converted to sugars by plants during photosynthesis. It is the primary source of organic matter production on Earth. GPP is also central to the carbon cycle and for understanding carbon feedbacks to climate. Currently, it exceeds ecosystem respiration (ER) and controls the overall direction of land carbon sequestration on a global scale, thus having a cooling effect on climate. However, carbon cycle–based terrestrial feedbacks in the future have substantial uncertainties and therefore represent one of the largest uncertainties in climate projections (1). A large source of this uncertainty stems from our inability to quantify GPP at large spatial scales and our incomplete understanding of the sensitivity of GPP to rising atmospheric CO_2 concentrations and air temperature (2, 3).

In the Arctic and Boreal regions, where climate warming has been magnified by more than a factor of 2 relative to other regions of the globe (4, 5), the growth of GPP is thought to have contributed to an increase in the atmospheric CO_2 mole fraction seasonal cycle amplitude (SCA) observed over the northern high latitudes (6, 7), either due to an earlier onset or lengthening of the growing season (6, 8, 9) or enhanced carbon uptake (7, 10), although increased respiration (11, 12) and transport from midlatitudes (13, 14) also contribute.

Despite the vital role of GPP in the carbon cycle, climate, and food systems, its magnitudes and trends over the Arctic and Boreal regions are poorly known. Annual GPP estimated from terrestrial ecosystem models (TEMs) and machine learning

Significance

Interactions between terrestrial carbon dioxide (CO_2) fluxes and climate or terrestrial ecosystem feedbacks exert a large uncertainty in climate projections. This uncertainty arises in part from poor quantification of gross CO_2 fluxes and their sensitivity to climate change over large spatial scales. Here, we demonstrate the usefulness of carbonyl sulfide (COS) for quantifying photosynthetic CO_2 uptake in the Arctic and Boreal ecosystems despite uncertainties in COS sources and sinks. The results highlight how the combination of atmospheric COS and CO_2 observations provides insights into past terrestrial ecosystem changes and can be utilized as a tool for direct quantification of these feedbacks impacted by climate change over the Arctic and Boreal ecosystems in the future.

Author contributions: L.H., S.A.M., A.E.A., C.S., and J.M. designed the analysis; L.H. developed CT-L-COS and conducted inversions; S.A.M. led the COS measurements and provided substantial input on the analyses; A.K. conducted the SiB4 runs with advice from J.M., I.T.B., and S.D.; A.K. helped with the construction of gridded LRU estimates; A.E.A. led the NOAA tower sampling network, CT-L footprints computation, and the CT-L CO_2 core code development; C.S. led the NOAA aircraft sampling network; E.C., Y.P.S., M.E.W., and P.S. provided COS anthropogenic, soil, and ocean flux products; P.T. led the establishment of the NOAA North American tower and aircraft sampling network; M.C.S. and M.C. conducted COS measurements; K.M. conducted aircraft data QA/QC; K.T. contributed to the CT-L CO_2 core code development and helped with background estimation; B.H. led the calibration of NOAA COS measurements; J.W.E. oversaw the NOAA Halocarbons & other Atmospheric Trace Species (HATS) group; I.V. provided Perseus GCMS COS data; and L.H. wrote the paper with edits and input from all authors, especially from S.A.M., C.S., and J.M.

The authors declare no competing interest.

This article is a PNAS Direct Submission. A.A. is a guest editor invited by the Editorial Board.

[1]To whom correspondence may be addressed. Email: lei.hu@noaa.gov.

This article contains supporting information online at https://www.pnas.org/lookup/suppl/doi:10.1073/pnas.2103423118/-/DCSupplemental.

Published November 8, 2021.

methods (15, 16) differ by as much as a factor of 6 (Fig. 1 and Table 1), and their estimated trends over the past century vary by 10 to 50% over the North American Arctic and Boreal region for the TEMs participating in the Multiscale Synthesis and Terrestrial Model Intercomparison Project (MsTMIP) (*SI Appendix*, Fig. S1). Given this large uncertainty, the current capability for constraining GPP on regional scales remains very limited. No direct GPP measurements can be made at scales larger than at a leaf level, because the basic process of GPP, which extracts CO_2 from the atmosphere, is countered by the production of CO_2 for respiration. Although large-scale GPP estimates have been made by machine learning methods (15, 16), light-use efficiency models (17), empirical models (18), and terrestrial biogeochemical process models (19–21) that have been trained on small-scale net CO_2 fluxes measured by eddy covariance towers, they substantially differ in mean magnitude, interannual variability, trends, and spatial distributions of inferred GPP (22–24). Satellite remote-sensing measurements of solar-induced chlorophyll fluorescence (SIF) and near-infrared reflectance of vegetation (NIRv) have been strongly linked to GPP on regional and global seasonal scales (25–28). However, GPP estimates based on scaling of SIF and NIRv can be limited by inconsistent and poorly constrained scaling factors among different plant functional types (29) or can be biased from interferences of clouds and aerosols in retrievals (30).

Recently, carbonyl sulfide (COS) has emerged as a promising new tracer for constraining large-scale GPP trends and spatial distributions (23, 32), as COS is taken up together with CO_2 by plants during photosynthesis (33–35). Unlike CO_2, for which uptake is reversible via respiration, COS is irreversibly hydrolyzed inside leaves, resulting in a unidirectional plant uptake. However, COS is a trace gas that has multiple sources and sinks. The "missing" global source (i.e., the imbalance between total sources and sinks) (34, 36, 37) and the poor characterization of its various surface fluxes, whether they are related or unrelated to photosynthetic processes (37–40), have limited the wide application of COS for direct quantification of GPP. Furthermore, uncertainties associated with leaf relative uptake ratios (LRUs) between COS and CO_2 (41, 42) further complicate this application.

In this study, we derive regional GPP over the North American Arctic and Boreal region with atmospheric COS measurements and carefully consider all of these uncertainties. We used atmospheric COS measurements from the US National Oceanic and Atmospheric Administration (NOAA)'s Global Greenhouse Gas Reference Network during 2009 to 2013 to directly quantify regional GPP from inverse modeling of atmospheric COS observations over the Arctic and Boreal North America (*Methods*).

Table 1. Annual COS fluxes and GPP over the North American ABR, estimated from process-based bottom-up approaches and our atmosphere-based top-down method

	Process-based estimates	This study
GgS/y		
Net COS fluxes	−19	−28 (−38 to −20)
Anthropogenic	0.2*	0.1 (0.05 to 0.15)
Biomass burning	4.1[†]	1.8 (0.5 to 4.1)
Soil	−3.9 (−4.2 to −3.6)[†]	−2.8 (−4.2 to −2.2)
Plant (total)	−19[‡]	−27 (−35 to −22)
Plant (daytime)	−17[‡]	−23 (−30 to −18)
PgC/y		
GPP	1.5 to 9.7[§]	3.6 (2.1 to 6.2)

The uncertainty ranges from this study include the full ensemble plus 2σ errors derived from individual inversions.
*From Zumkehr et al. (31).
[†]*Methods*.
[‡]From SiB4.
[§]From MsTMIP, SiB4, FluxCom (15), and FluxSat (16).

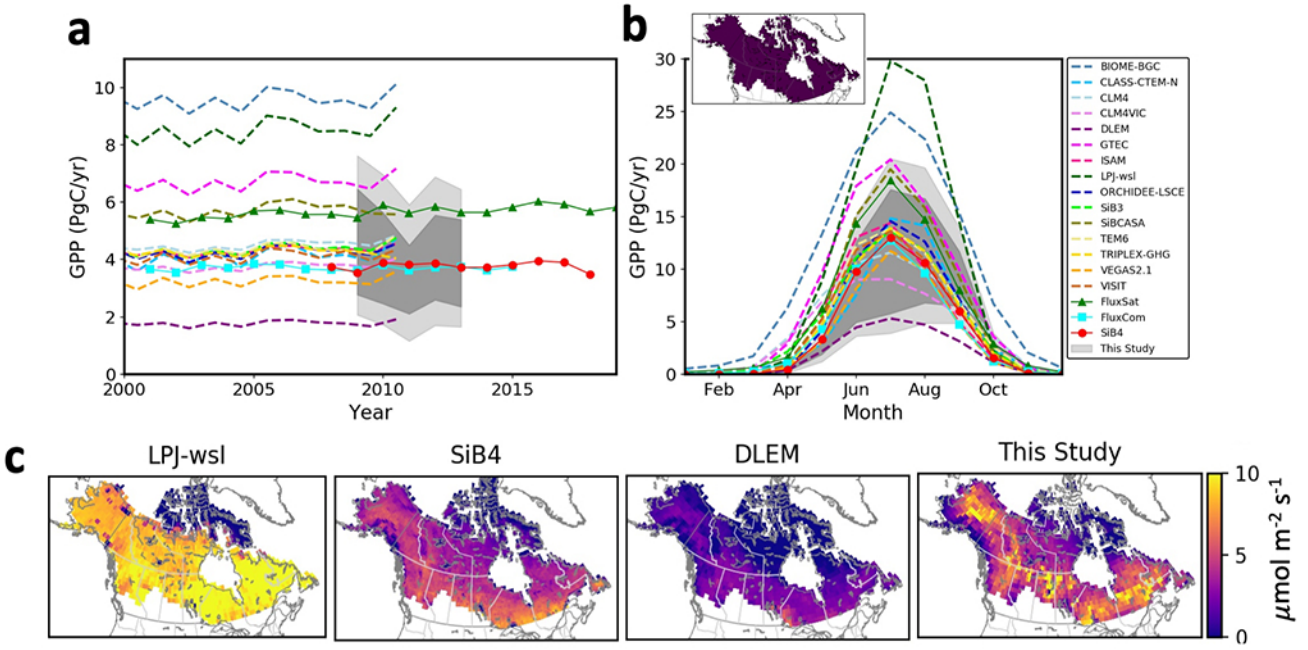

Fig. 1. Regional GPP for the North American ABR, estimated from bottom-up terrestrial models participating in Multiscale Synthesis and Terrestrial Model Intercomparison Project (MsTMIP) (dashed lines), FluxCom (cyan squares with solid lines), FluxSat (green triangles with solid lines), and SiB4 (red circles with solid lines) and our top-down atmospheric COS inversions (dark gray shading indicates the 2.5th to 97.5th of our best inversion ensemble estimates, whereas the light gray shading denotes the range of our best ensemble estimates plus 2σ uncertainties from each inversion). The North American ABR is indicated in *B*. (*A*) Annual GPP estimates between 2000 and 2019. (*B*) Multiyear average seasonal cycle of GPP from MsTMIP (2008–2010), FluxSat (2001–2019), FluxCom (2001–2018), SiB4 (2009–2013), and this study (2009–2013). (*C*) Spatial distribution of GPP in July 2010 from three selected TEMs (LPJ-wsl, SiB4, and DLEM) and average GPP from July in 2009 to 2013 derived from COS-based inversions. The spatial distribution of GPP from other TEMs is shown in *SI Appendix*, Fig. S12.

We estimated an ensemble of 54 time and space varying estimates of GPP using the daytime portion of plant COS uptake derived from each inversion and then converted to GPP using LRUs (*Methods*). The ensemble was generated considering three different representations of COS mole fractions in air entering the model domain (*SI Appendix*, Fig. S2) (so called "background mole fractions") that were presubtracted from atmospheric mole fraction observations before the inversions, multiple representations of anthropogenic and biomass burning emissions, soil fluxes, and LRUs (*Methods*). Here, we discuss the implications of the inferred magnitudes, spatial and seasonal variation, and trends of COS fluxes and GPP over a region that has experienced accelerated warming relative to the lower latitudes during the past few decades.

Results and Discussion

COS Fluxes. Atmospheric COS observations over the Arctic and Boreal North America reflect a strong dominance of surface uptake signal, indicated as negative vertical gradients in the aircraft profiles and surface depletions in COS mole fractions relative to those measured in the free troposphere or upwind background atmosphere, especially during summer and fall (June through September) (Fig. 2 and *SI Appendix*, Fig. S3). As a result, the derived annual net COS fluxes estimated from atmospheric COS inversions were −28 (−38 to −20) GgS · y^{-1} between 2009 and 2013 over the Arctic and Boreal North America (Table 1), with the largest uptake in June through September (*SI Appendix*, Fig. S4). The uncertainty in the derived net COS fluxes indicated above includes not only the 2σ statistical uncertainty derived from each individual inversion but also the range of estimates derived using different background estimations. Note that the estimated regional net flux is relatively insensitive to the prior assumptions in the inverse modeling analysis, as the result was fairly consistent, even when we used a prior with no flux variations in space or time (a "flat" prior) (*SI Appendix*, Fig. S4).

The atmosphere-derived net COS flux is primarily dominated by plant uptake of COS. The derived annual plant uptake from atmospheric COS inversions was −27 (−35 to −22) GgS · y^{-1}, given the range of anthropogenic, biomass burning, and soil fluxes we considered (Table 1 and Fig. 3 and *SI Appendix*, Figs. S5 and S6). The estimated plant COS uptake shows a strong seasonal cycle with near-zero flux in winter and a flux of −110 to −60 GgS · y^{-1} in summer (Fig. 3 and *SI Appendix*, Figs. S5 and S6). This plant COS uptake is composed of daytime and nighttime plant uptake (Fig. 3 and *SI Appendix*, Fig. S5). Although the daytime COS plant uptake is directly linked to photosynthetic activities, nighttime plant uptake of COS is not associated with photosynthesis and is likely due to incomplete closure of stomata that leads to light-independent COS hydrolysis catalyzed by the enzyme carbonic anhydrase (40, 42, 43). If total COS plant uptake is converted to GPP without distinguishing daytime versus nighttime fluxes, GPP would be overestimated by 5 to 15% in April through September and 30 to 50% in October through March over the North American Arctic and Boreal region (Fig. 3 and Table 1 and *SI Appendix*, Fig. S5).

The derived annual mean plant uptake of COS from atmospheric observations, −27 (−35 to −22) GgS · y^{-1}, is about 40% higher than simulated by the TEM Simple Biosphere Model version 4.2 (SiB4) (Table 1). The plant COS uptake simulated by SiB4 is close to the lower limit of plant COS uptake inferred from atmospheric observations between January and August and is smaller than the lower limit during September to December (Fig. 3). A forward model analysis using plant COS fluxes simulated by SiB4 would overestimate the atmospheric COS mole fractions all year around and especially during fall (*SI Appendix*, Figs. S7 and S8), whereas simulations with posterior fluxes derived from our COS inversions show improved agreement with atmospheric observations with a stronger correlation and smaller biases (*SI Appendix*, Figs. S7 and S8).

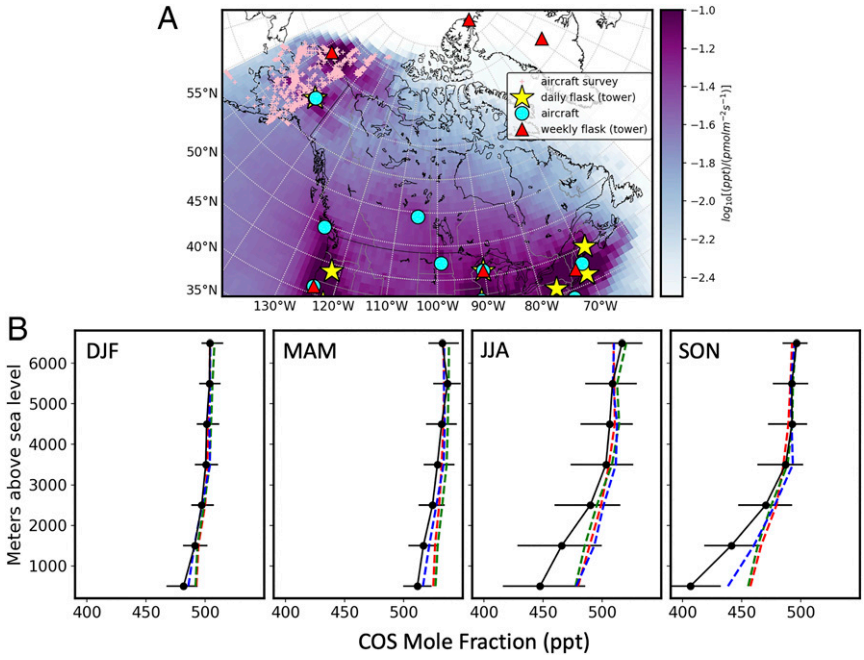

Fig. 2. NOAA's atmospheric COS mole fraction observations in the mid and high latitudes of North America. (*A*) Regular flask-air samples from towers (daily and weekly) and aircraft flights (biweekly to monthly). Color shading indicates average footprint sensitivity (in a log10 scale) of COS observations to surface fluxes during 2009 to 2013. (*B*) Seasonal average aircraft profiles at sites above 40°N (*Left* and *Right*: December to February, March to May, June to August, and September to November). Black symbols represent observed median mole fractions within each season and each altitude range with error bars indicating the 25th to 75th percentiles of the observed mole fractions. Colored dash lines denote median mole fractions of three different background (upwind) estimates in each season.

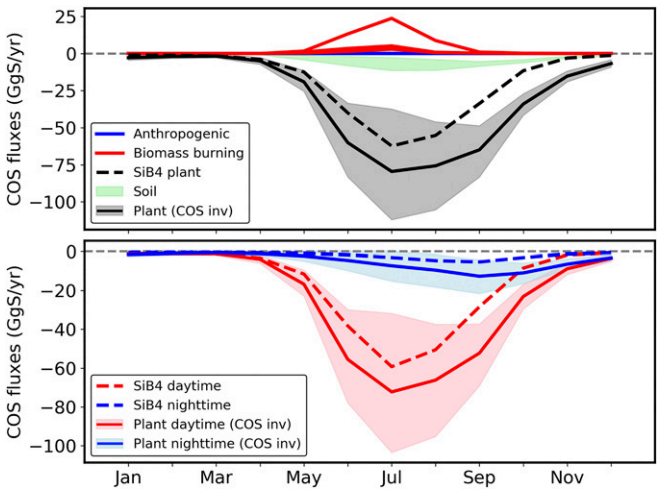

Fig. 3. Multiyear average monthly COS fluxes between 2009 and 2013 from anthropogenic sources, biomass burning, and plant and soil fluxes used and derived from this study for the North American ABR. (*Upper*) Multiyear average monthly anthropogenic COS fluxes (blue lines), biomass burning COS fluxes (red lines), soil COS fluxes (green shading), and plant COS fluxes simulated from SiB4 (black dashed line) and derived from this study (gray shading). Multiple lines with the same color indicate multiple different estimates. (*Lower*) The daytime and nighttime plant uptake derived from this study (a red solid line with light red shading and a blue solid line with light blue shading) and from SiB4 (red and blue dashed lines).

GPP. The COS-based monthly GPP derived from multiplying the daytime COS plant fluxes with LRUs (*Methods*) shows significant correlation with the contiguous SIF (CSIF) (44) and the Moderate Resolution Imaging Spectroradiometer NIRv (26) (Fig. 4*A*) over the North American Arctic and Boreal region in both space and time at a 99% CI. The correlation coefficients between the COS-derived monthly total GPP and monthly area-weighted average CSIF and NIRv are 0.92 and 0.95 on a regional scale (Fig. 4*C*). Their spatial correlations are greater than 0.7 when aggregating GPP, CSIF, and NIRv to 2° × 2° or higher. The timing for the start of the seasonal cycle (SOS) and end of the seasonal cycle (EOS) is similar between the COS-based GPP and monthly area-weighted CSIF for all 5 y considered in this study (Fig. 4). Although the SOS of NIRv is similar to the COS-based GPP estimates and CSIF, the EOS of NIRv is about 1 mo delayed (Fig. 4).

We also found agreement between our COS-based GPP to GPP estimated from available eddy covariance flux towers in our domain. Because of the sparse atmospheric COS measurement network in this region, inversion fluxes on a grid scale are highly uncertain (*SI Appendix*, Fig. S9). Hence, we don't expect to be able to constrain fluxes at the fine spatial scale to which flux towers are sensitive and do not compare fluxes at single-flux towers. Instead, we extracted and averaged monthly fluxes at 15 $1^o \times 1^o$ grid cells in which there is a GPP estimate reported from flux towers in the FLUXNET and AmeriFlux networks over the North American Arctic and Boreal region. Our atmospherically derived GPP generally agrees well (90% of the time) with eddy covariance flux tower inferred average GPP (*SI Appendix*, Fig. S10), further supporting the validity of our COS-based approach.

Our best estimate of annual total GPP was 3.6 (2.4 to 5.5) PgC · y^{-1} over the Arctic and Boreal North America between 2009 and 2013 (Fig. 1), considering the 2.5th–97.5th percentile of 5-y average annual total GPP from the 36 ensemble members. Here, the 36 ensemble members only include the ones estimated from a temporally varying LRU approach (*Methods*). This is because when we consider a temporally constant LRU approach (1.68 for C3 plants and 1.21 for C4 plants), the correlation between the COS-derived monthly total GPP and monthly area-weighted average CSIF and NIRv was slightly lower. Annual GPP derived using a constant LRU approach is biased high by 10 to 70% than when derived from temporally varying LRU values due to higher GPP in the early morning and late afternoon during late spring through summer and all times during fall through early spring (*SI Appendix*, Fig. S11). This finding is consistent with a previous study (41) that considers eddy covariance measurements of CO_2 and COS. Hereafter, we only discuss the 36 GPP ensemble estimates derived from the two temporally varying LRU approaches. If we consider the 2σ error from each ensemble member, the full uncertainty of our COS-based annual GPP estimate would be 2.1 to 6.1 PgC · y^{-1}. The uncertainty of our GPP estimate is about half of the GPP range estimated from terrestrial models over this region (1.5 to 9.7 PgC · y^{-1}) (Table 1 and Fig. 1). Annual GPP estimates from terrestrial models such as the Lund-Potsdam-Jena Wald Schnee and Landshaft model (LPJ-wsl), the BioGeochemical Cycles model (BIOME-BGC), the Global Terrestrial Ecosystem Carbon model (GTEC), the Simple Biosphere/Carnegie-Ames-Stanford Approach (SiB-CASA), and FluxSat are close to or higher than the upper limit of our COS-based annual GPP estimates, whereas the the Dynamic Land Ecosystem Model (DLEM) simulation is near the lower limit (Fig. 1). In particular, our results suggest that TEMs such as LPJ-wsl and BIOME-BGC likely overestimate the annual GPP magnitudes and the seasonal cycle, provided that GPP from these two models are much larger than the upper limit of our annual estimate, and our uncertainty estimate considers a large range of possible errors associated with the COS-based inference of GPP. In contrast, GPP simulated by TEMs such as the Organizing Carbon and Hydrology in Dynamic Ecosystems model (ORCHIDEE), SiB4, the Community Land Model version 4 (CLM4), the Integrated Science Assessment Model (ISAM), version 6 of the Terrestrial Ecosystem Model (TEM6), the TRIPLEX-GHG model, the Vegetation Global Atmosphere Soils model (VEGAS), and FluxCom shows similar annual magnitudes (Fig. 1*A*) and seasonal variation (Fig. 1*B*) as derived from atmospheric COS observations; among these TEMs, ORCHIDEE and SiB4 display spatial distributions most similar to that derived from COS in July (*SI Appendix*, Figs. S12 and S13) with the smallest root mean square errors (RMSEs) and the strongest correlations with COS-derived GPP. Note that GPP simulated using SiB4 is not independent from our COS-observation-based GPP estimate, given that the SiB4-simulated COS fluxes were used in the construction of the prior COS flux for our inversions (*Methods*).

Implications. In the past seven decades, the increase of surface temperature in the Arctic has been more than two times larger than in lower latitudes (4, 5). During this period, observations suggest a concurrent increase in the SCA measured for atmospheric CO_2 mole fraction in the northern high latitudes that is about a factor of 2 larger than the increase of SCA of atmospheric CO_2 observed in the tropics. This has been primarily attributed to increasing GPP (7, 9, 10, 45) and respiration (11, 12) in the northern mid- and high latitudes (46). However, the magnitudes of increases in GPP and respiration and their relative contributions to the enhanced high-latitude CO_2 mole fraction SCA have been uncertain. The only way to further understand this problem is to first establish a robust capability for separately and accurately quantifying GPP and ER that are representative of a large regional scale.

With COS-derived regional GPP estimates for the North American Arctic and Boreal regions, we calculated regional ER by combining GPP with net ecosystem exchange (NEE) derived from our previous CarbonTracker-Lagrange CO_2 inversion (47) (Fig. 5). The derived regional monthly total ER is slightly smaller than regional monthly total GPP during late spring through summer, although the magnitude of their difference is not statistically significant considering their uncertainties (Fig. 5). The monthly total ER is significantly higher than GPP during mid-fall

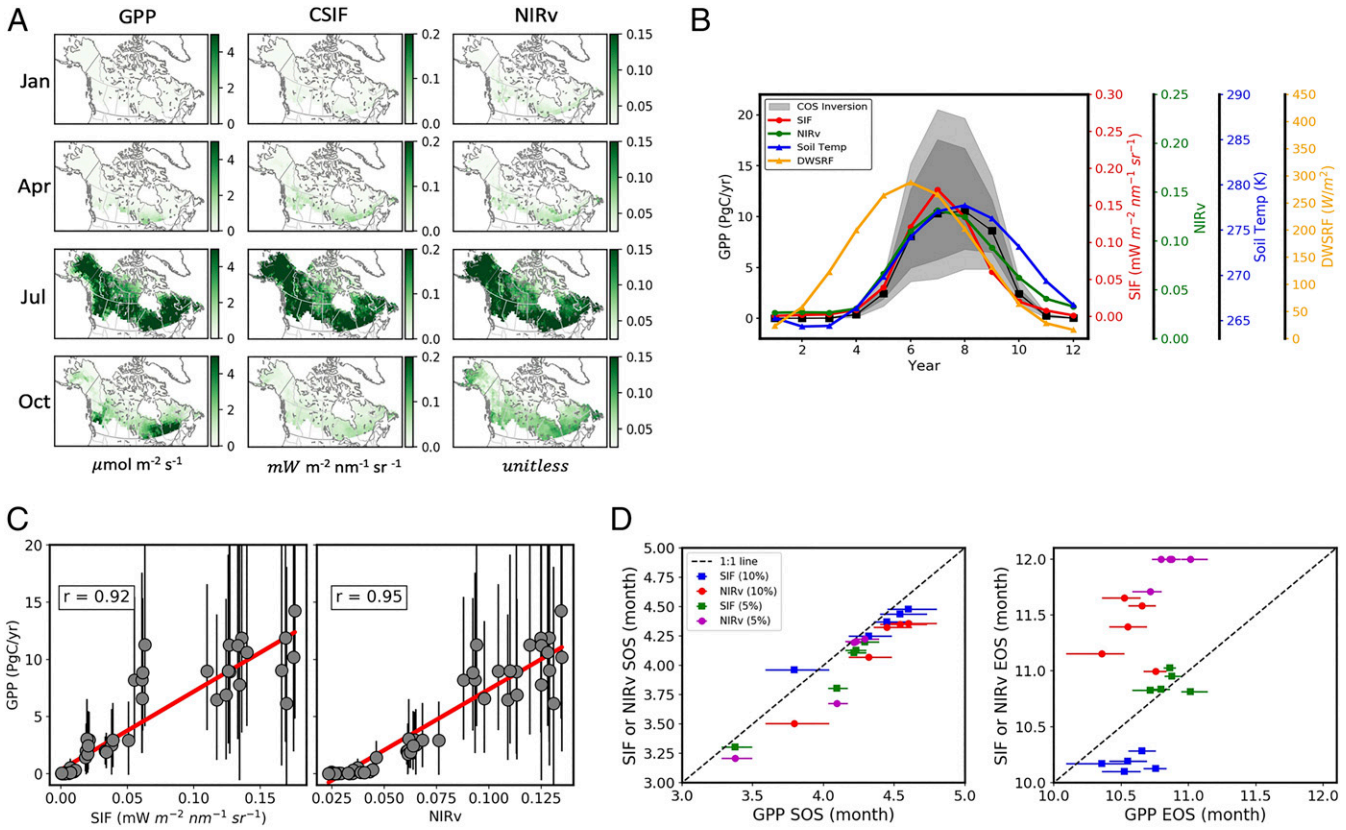

Fig. 4. Comparison of COS inversion-estimated GPP with the CSIF (46), NIRv (24), soil temperature (Soil Temp), and downward shortwave radiation flux (DWSRF). (*A*) Spatial maps of monthly GPP derived from atmospheric COS observations, CSIF, and NIRv averaged between 2009 and 2013 for January, April, July, and October. (*B*) Monthly estimates of GPP estimated from COS inversions and monthly area-weighted average CSIF, NIRv, Soil Temp, and DWSRF over the North American ABR, averaged between 2009 and 2013. The dark gray shading indicates the 2.5th to 97.5th percentile range of the best estimates from our inversion ensembles, whereas the light gray shading indicates the range of our inversion ensemble estimates plus 2σ uncertainties from each inversion. The black symbols connected by a black line denote multiyear average monthly mean GPP from all COS ensemble inversions. (*C*) Scatter plots between COS-based monthly GPP estimates and monthly area-weighted average CSIF or NIRv over the North American ABR for all months of the year. (*D*) The calculated SOS and EOS inferred from CSIF and NIRv versus the SOS and EOS indicated by COS-based GPP between 2009 and 2013. The values at 5% or 10% above their seasonal minima relative to their seasonal maxima were used as thresholds for calculating the SOS or EOS in each year (*Methods*).

through mid-spring (Oct through Apr). Correlation coefficients between monthly total GPP and monthly total ER across all seasons is 0.93.

Interestingly, the seasonal cycle and spatial distribution of our atmosphere-based monthly estimates of GPP and ER over the North American Arctic and Boreal region show strong correlations with air temperature and soil temperature (Fig. 5). The correlation coefficient between monthly total GPP and area-weighted average air or soil temperature is >0.89 during April through November (the start to end of the GPP seasonal cycle). If we further divide the GPP seasonal cycle into an increasing phase (April through July) and a decreasing phase (August through November), the slope between GPP and soil temperature during the decreasing phase is slightly larger than during the increasing phase (Fig. 5*B*), likely due to a strong limitation of solar radiation on GPP in autumn (Fig. 4*B*). Here, we used the downward shortwave radiation flux to examine the availability of solar radiation over this region. In April through July, the correlation between GPP and solar radiation is relatively low (r = 0.67) (*SI Appendix*, Table S1) compared to the correlation between GPP and air or soil temperature. When removing the effect of the covariation between radiation and temperature, the partial correlation (48) between GPP and solar radiation becomes statistically insignificant for April through July, whereas the partial correlation between GPP and air or soil temperature is statistically significant at a 95% CI even when solar radiation is controlled (*SI Appendix*, Table S2). This is because starting in January, solar radiation begins increasing over this region. By April, the average solar radiation in this region has already increased to two-thirds of its annual maximum (Fig. 4*B* and *SI Appendix*, Fig. S14). Solar radiation is likely no longer a limiting factor in plant growth over this area, whereas plant growth is more restricted by temperature in April, especially by soil temperature. This is further supported by a strong correlation between soil temperature in April and the SOS of GPP (r = 0.98) (*SI Appendix*, Fig. S15). As the year continues, solar radiation reaches its maximum in June and starts to decrease thereafter. By September, the first month after GPP starts to decrease, the average solar radiation has dropped below the level in April, whereas air and soil temperatures are comparable to those in July (Fig. 4 and *SI Appendix*, Fig. S14). Thus, the decreasing regional total GPP in August through November is likely strongly driven by limited and decreasing solar radiation. This is further supported by stronger correlation between GPP and solar radiation in August through November (r = 0.95). Decreasing solar radiation further results in declining air temperature and soil temperature, which will further facilitate the decrease of GPP in the fall. Although soil moisture is also at the minimum in August through September, it is not likely to be the dominant factor governing the decrease of GPP in the fall. This is because when soil moisture increases in the fall, there is a continued decrease of GPP. However, GPP and soil moisture are indeed

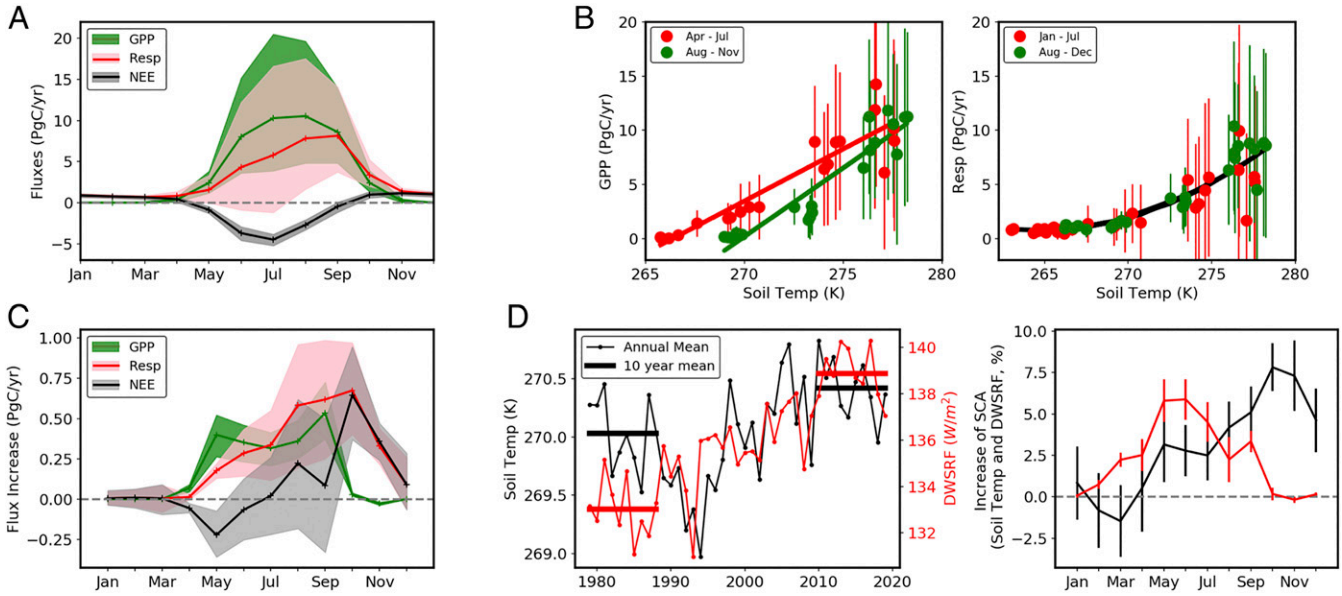

Fig. 5. The atmosphere-based estimates of the multiyear average seasonal cycle of GPP, ER, and NEE and estimation of their warming-induced seasonal cycle amplification over the North American ABR. (*A*) Multiyear average monthly GPP, ER ("Resp" as labeled in the figure), and NEE between 2009 and 2013 over the North American ABR. The solid lines represent the ensemble means, whereas the color shadings indicate their uncertainties. (*B*) Relationship between monthly GPP and ER derived from this study and monthly area-weighted soil temperature (Soil Temp) over North American ABR. The solid lines represent a linear fit between GPP and soil temperature for April to July (red) and August to November (green) and a quadratic regression between ER and soil temperature for all months. (*C*) Estimated increases of GPP, ER, and NEE from 1979 to 1988 and 2010 to 2019 over the North American ABR. The color shading represents our estimation errors, constructed from 100 ensemble empirical relationships of GPP/ER with Soil Temp and DWSRF, considering the uncertainty of our monthly GPP and ER estimates shown in *A*. (*D*) Annual Soil Temp and DWSRF (*Left*) and monthly Soil Temp and DWSRF increases between 1979 and 1988 and 2010 and 2019. The error bars represent the sum of SEs of the monthly means between 1979 and 1988 and 2010 and 2019. The monthly increases of Soil Temp and DWSRF and their errors were normalized relative to the average SCA in 1979 and 1988.

anticorrelated in this analysis (*SI Appendix*, Tables S1 and S2), likely due to loss of soil water through transpiration.

The seasonal cycle of ER derived here is most strongly correlated with temperature, especially soil temperature (*SI Appendix*, Table S1). Unlike GPP, the ER–temperature relationship we derived is not influenced by solar radiation (Fig. 5), as it falls into one quadratic relationship for all months. After temperature and radiation, GPP and ER anti-correlate with snow cover and positively correlate with precipitation (*SI Appendix*, Table S1), but their correlations are due to the covariations of snow cover and precipitation with temperature (*SI Appendix*, Fig. S14). When the effect of their covariation was removed, the partial correlations of snow cover and precipitation with GPP and ER were statistically insignificant (*SI Appendix*, Table S2). A strong temperature control of carbon dynamics in the northern high latitudes has been suggested in earlier studies with satellite remote-sensing–based land observations (11, 22, 45, 49, 50). Our results suggest that both temperature and solar radiation are important in regulating carbon fluxes in northern high-latitude terrestrial ecosystems.

To estimate the impact of past changes in climate on the seasonal cycle of GPP, ER, and NEE in the North American Arctic and Boreal region, we first built empirical models to simulate the seasonal cycle of GPP and ER with climate variables and inversion results during 2009 through 2013 (*Methods*). The best empirical model to simulate monthly regional total GPP among the 30 empirical models we considered is a linear model between GPP and soil temperature for April through July and between GPP and solar radiation for August through November (*SI Appendix*, Table S3), whereas monthly regional total ER can be best simulated with a quadratic relationship with soil temperature (*SI Appendix*, Table S4) (*Methods*). Liu et al. (50) demonstrated that the relationship between the fraction of Photosynthetically Active Radiation (fPAR) and temperature is relatively constant in the northern high latitudes over the past several decades. Because fPAR strongly influences GPP (50), we also assumed here that the empirical relationship between the seasonal cycle of GPP and ER with climate variables derived for 2009 through 2013 holds over time. We then estimated the likely changes in the climatological seasonal cycle of GPP and ER from 1979 through 1988 to 2010 through 2019 based on the long-term changes of soil temperature and solar radiation over the North American Arctic and Boreal region. From 1979 through 1988 to 2010 through 2019, the annual soil temperature increased by 0.5 K with larger warming in autumn (September through December) (Fig. 5). The autumn soil temperature rise (~1 K) is equivalent to ~8% of the SCA of the area-weighted average soil temperature over the North American Arctic and Boreal region (Fig. 5). Our analysis suggests that the increase of soil temperature directly enhances ER, especially in autumn, whereas it results in an increase of GPP in spring through early summer (Fig. 5). Because GPP is more sensitive to temperature changes in April through July than ER (Fig. 5*B*), the enhancement of GPP exceeds the increase of ER in spring through early summer due to warming in the past several decades (Fig. 5), resulting in an earlier onset of the growing season and increased net carbon uptake. In autumn, as regional GPP is largely limited by solar radiation and solar radiation has increased much less than soil temperature relative to their SCA (*SI Appendix*, Table S1), the warming-induced increase of GPP is less than ER during this season (Fig. 5), which can cause an earlier zero-crossing day for NEE and an increase in net carbon emission in autumn over this region. These phenomena have already been observed in atmospheric CO_2 measurements made at Barrow, Alaska (11, 12). The increases in net carbon uptake in April through July could lead to a larger cumulative CO_2 uptake flux from the atmosphere and a deeper seasonal minimum in atmospheric CO_2 mole fractions,

whereas the enhancement of net carbon releases in August through December would lead to a larger cumulative CO_2 emission and an increase of maximum in atmospheric CO_2 seasonal cycle. Both effects would add to the enhanced SCA of atmospheric CO_2 in the northern high latitudes. Furthermore, our estimated increase of annual GPP is less than the increase of annual ER between 1979 through 1988 and 2010 through 2019, indicating the temperature rise over the past decades resulted in an overall enhancement of net carbon release to the atmosphere due to the autumn limitation of light on the warming-induced growth of GPP. Provided other factors do not become limiting, as the Arctic continues to warm, additional net carbon uptake in spring and net carbon release in autumn would amplify the atmospheric CO_2 SCA in the northern high latitudes additionally. If the warming continues to be more prominent in the dormant seasons, such warming might be expected to lead to increased net carbon emission and a positive climate feedback over this region.

These estimates of long-term warming-induced changes on GPP and ER in North American Arctic and Boreal region are derived on the basis of seasonal sensitivities of these fluxes to soil temperature and solar radiation during 2009 through 2013, assuming that these seasonal relationships are relevant for informing us about trends over decadal periods. With the probable CO_2 fertilization effect (51–53), the expansion of Arctic vegetation (54), and shifts of vegetation types driven by interactions of climate warming and fire (55), the overall increases of GPP and ER in the Arctic have likely been greater than that estimated here; however, such effects have been challenging to quantify, largely due to an inability to constrain regional-scale GPP. However, our study provides evidence for the usefulness of atmospheric COS observations for estimating large regional-scale GPP over the Arctic and Boreal area, despite the limitation of the current atmospheric COS sampling network in this region. Furthermore, our results suggest that future expansion of this observing system could afford us opportunities for direct quantification of interannual variability and trends of GPP and ER, thereby enhancing our understanding of the carbon cycle–climate feedback loops in this important region of the world.

Methods

Atmospheric COS Observations. The NOAA Global Monitoring Laboratory has been measuring atmospheric COS mole fractions in flask-air samples collected from 13 locations around the globe since 2000, with five sites located in North America. In 2006, North American COS measurements were augmented to include daily flask-air samples collected from 11 to 16 tower locations and every 2 to 4 wk at 16 regular aircraft profiling sites between 0 and 8 km above ground for determination of dry-air mole fraction of COS and other trace gases. Details on NOAA's COS flask-air sampling locations can be found at https://www.esrl.noaa.gov/gmd/dv/site/?program=hats&active=1.

The North American portion of NOAA flask-air sampling is based primarily on programmable flask packages (PFPs) composed of 12 0.7-L borosilicate glass flasks (56, 57). Once filled with sample air, PFPs are shipped to our Boulder, CO, laboratory and analyzed by one dedicated Gas Chromatography and Mass Spectrometry (GCMS) instrument (called "M2," which was later upgraded to "PR1" in September 2014). Median analysis precision for M2 COS measurements during 2009 to 2013 was ~1 ppt (picomole COS per mole dry air); in 95% of the analyses, it was less than 6 ppt. Long-term reproducibility of the flask measurements is roughly 6 ppt. This long-term reproducibility was determined by repeated measurements for air samples drawn from a suite of archived air tanks throughout the measurement record period.

Samples from our 13 global stations (five in North America) were collected in individual borosilicate flasks (2.2 L) or electropolished stainless steel (SS) flasks (2.5 to 3 L) (34). These flask-air samples were analyzed by another dedicated GCMS instrument (called "M1," which was upgraded to "M3" in mid-2009). Prior to mid-2009, the median replicate injection precision for COS at ambient levels with our instrumentation was 0.4%; 95% of the time it was <1.3% (i.e., <6.3 ppt). After mid-2009, median replicate precision was 0.2%, and 95% of the time, it was <0.75%.

Because we used atmospheric COS measurements that were primarily made by two different GCMS instruments (M1/M3 and M2) and different sampling flask types (PFPs and individual glass or SS flasks), any differences associated with different sampling flask types or analytical systems need to be corrected to avoid measurement differences biasing inversion fluxes. We compared COS measurements made from PFPs versus individual SS flasks collected at Park Falls, Wisconsin. The mean ratio of COS mole fractions measured in air collected in these two different types of flasks when sampled within 1 d of each other is 1.001 ($n = 140$; 1 $\sigma = 0.045$), indicating no statistical difference between measurements from both types of flasks (*SI Appendix*, Fig. S16). Furthermore, we have compared results from a subset of flask-air samples collected from our global network that were analyzed on both of the GCMS instruments. Their mean ratios of COS mole fractions measured by M3 and M2 between 2009 and 2013 is 0.998 ($n = 319$; 1 $\sigma = 0.012$) except with up to a 2% difference in 2012 to 2013 (*SI Appendix*, Fig. S17). To ensure a consistent measurement scale, we correct all the M2 measurements to the M3 scale to be consistent with data used in previous COS publications (32, 34).

Regional Inverse Modeling of Atmospheric COS Mole Fraction Observations. We converted the COS mole fraction information measured by atmospheric measurements to surface COS fluxes using a regional inverse modeling system, CarbonTracker-Lagrange-COS, CT-L-COS. The CT-L-COS modeling system is modified and adapted from the CarbonTracker-Lagrange CO_2 inverse modeling framework (47). CT-L uses the high-resolution Weather Research and Forecasting–Stochastic Time-Inverted Lagrangian Transport (WRF-STILT) model (58) to quantify the relationship between COS mole fraction enhancements or depletions to upwind fluxes. It solves for 8 scaling factors per wk for each 1° × 1° grid cell flux, one for each 3-hourly time of day (i.e., a weekly average adjustment to the diurnal cycle). Different from the CT-L CO_2 system, we augmented the inversion domain to include ocean grid cells adjacent to the North American land (*SI Appendix*, Fig. S2). We did this to include the influence of oceanic fluxes to the atmospheric observations near the coast and reduce edge effects, as oceanic COS emissions are significant in the atmospheric COS budget (59). Because of the expansion of the inversion domain and increases in the spatial dimension of the state vector in the inversion, we had to reduce the batch inversion window from 1 y to 6 mo to make the batch inversion more computationally manageable. In each batch inversion, we discarded the first and last month of fluxes to remove potential "end effects" in those two months.

The prior 1° × 1° net COS fluxes included in the COS inversion were computed based on a linear combination of inventory- or process-based estimates of anthropogenic COS emissions (31), biomass burning emissions (60, 61), ocean fluxes (62), and terrestrial ecosystem fluxes (plant and soil fluxes) from the SiB4 (63) (*SI Appendix*, Fig. S6). The sector-based linear scaling factors (β) (*SI Appendix*, Fig. S6) were calculated based on a method similar to the calculation of drifting coefficients in the deterministic model in a geostatistical inverse modeling framework (64–66) (Eq. **1**).

$$\beta = \left(X^T H^T \Psi^{-1} H X\right)^{-1} X^T H^T \Psi^{-1} z, \quad [1]$$

where X is a matrix with sector-based COS fluxes; H denotes WRF-STILT footprints; $\Psi = HQH^T + R$, in which R and Q represent the model–data mismatch covariance matrix and the prior flux error covariance matrix; and z represents COS mole fraction deviations at North American continental sites relative to the upwind background atmosphere. We further used the Bayesian Information Criterion (BIC) (65, 66) to score a few possible combinations of sector-based COS fluxes and assess the necessity for the inclusion of all COS fluxes in the inversion domain. Our results suggest that consideration of all possible COS fluxes from within the inversion domain (from terrestrial ecosystems, anthropogenic sources, biomass burning, and ocean) best represents the observed COS variability in the atmosphere than neglecting any minor fluxes. We also considered using population density to represent the spatial distribution of anthropogenic fluxes of COS. However, the BIC test suggests using the anthropogenic COS fluxes constructed from Zumkehr et al. (31) is superior to using population density, as they better represent the atmospheric observations along with fluxes from other sectors. Furthermore, we also tested inversions conducted without scaling the sector-based fluxes, but this resulted in a poorer fit between simulations and observations in posterior fluxes than the inversion results considering scaling the sector fluxes.

With inversely modeled net COS fluxes and their uncertainties at each grid cell, we then subtracted the original or scaled fluxes from anthropogenic sources, biomass burning, and soil fluxes (described below) of COS to derive plant COS fluxes. Fluxes and flux uncertainties were aggregated to the North American Arctic and Boreal region by considering the posterior covariances in space and time for each inversion.

Background COS Mole Fraction Estimation. Background COS mole fractions were first subtracted from atmospheric observations to derive COS mole

fraction enhancement or depletion relative to the background atmosphere before the grid-scale inversion was performed. We used three different empirical methods similar to our previous inversion analyses for other atmospheric trace gases (47, 66–68) to derive COS background and evaluate the possible systematic biases in each individual background estimate (1). The first background approach ("bg_ht") considers COS mole fractions directly measured from the background atmosphere. This approach uses data collected from 0 to 1 km above sea level at remote marine locations and free tropospheric data that have low surface sensitivity from aircraft observations (https://www.esrl.noaa.gov/gmd/dv/site/?program=hats&active=1) to build a three-dimensional (3D) background field as a function of time, latitude, and altitude. To construct the 3D background field, we first divide data into three different vertical levels: 0 to 1 km, 2 to 5 km, and 5 to 8 km. A long-term trend and average seasonal cycle were fit with a function containing polynomial and harmonic terms to create a smoothed curve at each site and altitude bin (69). Interannual variability in the seasonal cycle, calculated from the detrended and deseasonalized residuals, was then added to the smoothed curve. Gap filling was performed based on the average seasonal cycle at each site and altitude bin. By fitting data extracted from the smoothed curve as a function of sine of latitudes at synchronized time steps from all sites, we built an evenly spaced and time-synchronized background surface across all latitudes for each altitude bin. The constructed background surfaces for the three altitude bins were further linearly interpolated between altitudes to get background estimates at a finer vertical resolution. From this 3D background, we extracted background COS mole fraction based on the sampling time, latitude, and altitude for each observation itself (2). The second background approach ("bg") considers the 3D background mole fractions built from the first approach and the WRF-STILT back-trajectories (47). Each background estimate for each observation is the average value of the sampled COS mole fractions from the 3D field at latitude, altitude, and time in which the 500 back-trajectory particles last exited the North American continent (*SI Appendix*, Fig. S2) horizontally or vertically (above 5 km above sea level). Any trajectories terminating within the continental boundary layer were assigned with a latitude- and altitude-dependent value from the 3D background field. This approach has the advantage of considering atmospheric transport and vertical mixing, but it may not capture synoptic variability, and it lacks an accurate representation of the continental boundary layer (3). The third background approach ("bg_corr") considers possible biases in the second approach due to under-representation in the 3D background itself, especially in the continental boundary layer, and transport uncertainties. In this approach, we consider any observations with summed footprints less than 1 ppt/(pmol m^{-2} s^{-1}) as background observations (47). We calculated the mean difference between observed and estimated background for this subset of observations by season, by altitude (0 to 3 km, 3 to 6 km, and 6 to 8 km), and by region (i.e., Arctic and Boreal North America, western temperate North America [130° to 108°W], midtemperate North America [108° to 86°W], and eastern temperate North America [86° to 64°W]. We then used this mean seasonal difference and applied a correction on our estimated background from the second approach by season, altitude, and region. The overall difference in the estimated background from these three approaches is shown in *SI Appendix*, Fig. S3.

Estimating Soil COS Fluxes. Soil COS fluxes were estimated by three different methods: 1) Soil COS fluxes were simulated by SiB4 (63) and 2) Soil COS fluxes were generated based on the empirical COS soil flux relationship with soil temperature and soil moisture (38) and the meteorological fields from the North American Regional Reanalysis. This empirical estimate was scaled to match the COS soil flux magnitude observed at Harvard Forest, Massachusetts (42). 3) Soil COS fluxes were also approximated as inversion-derived nighttime COS fluxes. Because it was observed that soil fluxes accounted for 34 to 40% of total nighttime COS uptake in a Boreal Forest in Finland (43), we assumed a similar fraction of soil fluxes in the total nighttime COS fluxes in the North American Arctic and Boreal region and similar soil COS fluxes in the day as the night. Soil fluxes derived from these three different approaches yielded an estimate of −4.2 to −2.2 GgS/y over the North American Arctic and Boreal region, accounting for ∼10% of the total ecosystem COS uptake.

Estimating GPP. The daytime portion of plant COS fluxes from multiple inversion ensembles (considering uncertainties in background, anthropogenic, biomass burning, and soil fluxes) was converted to GPP based on Eq. **2**:

$$GPP = -\frac{F_{COS}}{LRU}\frac{C_{a,CO_2}}{C_{a,COS}}, \quad [2]$$

where LRU represents leaf relative uptake ratios between COS and CO_2. C_{a,CO_2} and $C_{a,COS}$ denote ambient atmospheric CO_2 and COS mole fractions. Daytime here is identified as when PAR is greater than zero. LRU was estimated with three approaches: in the first approach, we used a constant LRU for C3 and a constant LRU for C4 plants compiled from historical chamber measurements. In this approach, the LRU value in each grid cell was calculated based on 1.68 for C3 plants and 1.21 for C4 plants (37) and weighted by the fraction of C3 versus C4 plants in each grid cell specified in SiB4. In the second approach, we calculated temporally and spatially varying LRUs based on Eq. **3**:

$$LRU = R_{s-c}\left[\left(1+\frac{g_{s,cos}}{g_{i,cos}}\right)\left(1-\frac{C_{i,c}}{C_{a,c}}\right)\right]^{-1}, \quad [3]$$

where R_{s-c} is the ratio of stomatal conductance for COS versus CO_2 (∼0.83); $g_{s,COS}$ and $g_{i,COS}$ represent the stomatal and internal conductance of COS; and $C_{i,C}$ and $C_{a,C}$ denote internal and ambient concentration of CO_2. The values for $g_{s,COS}$, $g_{i,COS}$, $C_{i,C}$, and $C_{a,C}$ are from the gridded SiB4 simulations. In the third approach, we scaled the simulated SiB4 LRU to better match chamber measurements under strong sunlight conditions (PAR > 600 $\mu mol\, m^{-2}\, s^{-1}$) when LRU is relatively constant (41, 42) for each grid cell. When converting COS fluxes to GPP, we used surface atmospheric CO_2 mole fractions simulated from the posterior four-dimensional (4D) mole fraction field in Carbon Tracker (CT2017) (70). We further estimated the gridded COS mole fractions based on the monthly median COS mole fractions observed below 1 km from our tower and airborne sampling network (Fig. 2). The monthly median COS mole fractions at individual sampling locations were extrapolated into space based on weighted averages from their monthly footprint sensitivities.

Constructing and Evaluating the Empirical GPP and ER Models. To establish an empirical relationship of GPP and ER seasonal cycle with climate variables, we considered 30 different empirical models for GPP (*SI Appendix*, Table S3) and 10 empirical models for ER (*SI Appendix*, Table S4) with different combinations of climate variables. We used the climate data from the North American Regional Reanalysis for this study. To select the best empirical model, we divided the atmosphere-based monthly GPP and ER estimates into one training set and one validation set. We used 4 y of monthly inverse estimates as our training set and 1 y of monthly inverse estimates as our independent validation set. We then iterated this process for five times; each time, we selected a different year as our validation set and the rest as our training set. In each iteration, we evaluated the performance of the empirical models by calculating the BIC score for the training set and RMSEs and correlations between simulated and inversely modeled monthly GPP or ER for the independent validation set. The reason to use a BIC score rather than using RMSE and correlations for the training set is that BIC not only considers how well the model fits the data but also applies penalties for adding additional fitting variables to avoid overfitting. The BIC score of each empirical model can be calculated from Eq. **4**:

$$BIC = -2L + p\,ln(n), \quad [4]$$

where L represents the log likelihood of the model, p represents the number of coefficients that need to be derived from the empirical model, and n denotes the number of data in the training set.

Assuming the errors between empirically simulated and inversely modeled monthly fluxes are a Gaussian distribution, we calculated the coefficients of each empirical model based on the least-squares method. The log likelihood of each model was calculated from Eq. **5**:

$$L = -\frac{n}{2}\ln(2\pi) - n\ln(s) - \frac{1}{2s^2}\sum_{i=1}^{n}\left(y_i - y_{sim,i}\right)^2, \quad [5]$$

where y represents the inversely modeled GPP or ER; y_{sim} denotes the simulated GPP or ER with the empirical model; and s represents the SD of the errors between y and y_{sim}.

For models with the same number of fitting parameters or coefficients, the lower the BIC score is, the larger the likelihood that the model is (Eq. **4**). The BIC scores for the training sets and RMSE and r^2 for the validation sets are presented in *SI Appendix*, Tables S3 and S4, which are the average BIC score and average RMSE and r^2 among the five iterations.

The best empirical model to simulate monthly regional total GPP among the 30 empirical models we considered is a linear model between GPP and soil temperature for April to July and between GPP and solar radiation for August to November (*SI Appendix*, Table S3), whereas monthly regional total ER can be best simulated with a quadratic relationship with soil temperature (*SI Appendix*, Table S4). The RMSE and r^2 between the atmosphere-derived and empirically simulated multiyear average seasonal cycle are 0.8 PgC · y^{-1} and 0.96 for GPP, whereas they are 0.7 PgC · y^{-1} and 0.94 for ER (*SI Appendix*, Fig. S18). We then extrapolate the selected empirical models to estimate changes

in the seasonal cycle of GPP and ER due to long-term changes of temperature and radiation over the North American Arctic and Boreal region.

Calculating the Timing for the SOS and EOS. The SOS and the EOS for the COS-based GPP, CSIF, and NIRv were calculated based on when these variables increased or decreased to a threshold each year. Here, we defined this threshold as a 5 to 10% increase between the monthly minimum and maximum GPP, CSIF, and NIRv averaged between 2009 and 2013.

Data Availability. NOAA atmospheric COS observations used in this analysis are available at https://doi.org/10.15138/q82j-7x17. Modeled footprint data are available at ftp://aftp.cmdl.noaa.gov/products/carbontracker/lagrange/footprints/ctl-na-v1.1. Inversely modeled fluxes and SiB4 fluxes are accessible at https://doi.org/10.15138/q82j-7x17. The SiB4 model code can be accessed at http://sib.atmos.colostate.edu/. Inverse modeling code is available at https://doi.org/10.15138/70v3-8344.

ACKNOWLEDGMENTS. This work is funded by the NASA Terrestrial Ecology Program (80NSSC19M0105). We thank our retired colleague B. Miller for his contribution to the North American COS measurements. We thank A. Jacobson and K. Schuldt for preparing CT2017s assimilated 4D CO_2 mole fraction field. CarbonTracker CT2017 results can be downloaded from the website at http://carbontracker.noaa.gov. We thank J. Kofler, J. Higgs, T. Newberger, S. Wolter, D. Neff, E. Moglia, and others for their work associated with flask-air sampling.

1. P. Friedlingstein *et al.*, Uncertainties in CMIP5 climate projections due to carbon cycle feedbacks. *J. Clim.* **27**, 511–526 (2014).
2. A. Arneth *et al.*, Terrestrial biogeochemical feedbacks in the climate system. *Nat. Geosci.* **3**, 525–532 (2010).
3. D. Schimel, B. B. Stephens, J. B. Fisher, Effect of increasing CO_2 on the terrestrial carbon cycle. *Proc. Natl. Acad. Sci. U.S.A.* **112**, 436–441 (2015).
4. J. Hansen, R. Ruedy, M. Sato, K. Lo, Global surface temperature change. *Rev. Geophys.* **48**, RG4004 (2010).
5. J. Blunden, D. S. Arndt, State of the climate in 2018. *Bull. Am. Meteorol. Soc.* **100**, Si-S306 (2019).
6. C. D. Keeling, J. F. S. Chin, T. P. Whorf, Increased activity of northern vegetation inferred from atmospheric CO_2 measurements. *Nature* **382**, 146 (1996).
7. H. D. Graven *et al.*, Enhanced seasonal exchange of CO_2 by northern ecosystems since 1960. *Science* **341**, 1085–1089 (2013).
8. J. T. Randerson, C. B. Field, I. Y. Fung, P. P. Tans, Increases in early season ecosystem uptake explain recent changes in the seasonal cycle of atmospheric CO_2 at high northern latitudes. *Geophys. Res. Lett.* **26**, 2765–2768 (1999).
9. R. B. Myneni, C. D. Keeling, C. J. Tucker, G. Asrar, R. R. Nemani, Increased plant growth in the northern high latitudes from 1981 to 1991. *Nature* **386**, 698–702 (1997).
10. M. Forkel *et al.*, Enhanced seasonal CO_2 exchange caused by amplified plant productivity in northern ecosystems. *Science* **351**, 696–699 (2016).
11. S. Piao *et al.*, Net carbon dioxide losses of northern ecosystems in response to autumn warming. *Nature* **451**, 49–52 (2008).
12. S.-J. Jeong *et al.*, Accelerating rates of Arctic carbon cycling revealed by long-term atmospheric CO_2 measurements. *Sci. Adv.* **4**, eaao1167 (2018).
13. N. Zeng *et al.*, Agricultural Green Revolution as a driver of increasing atmospheric CO_2 seasonal amplitude. *Nature* **515**, 394–397 (2014).
14. J. M. Gray *et al.*, Direct human influence on atmospheric CO_2 seasonality from increased cropland productivity. *Nature* **515**, 398–401 (2014).
15. M. Jung *et al.*, Scaling carbon fluxes from eddy covariance sites to globe: Synthesis and evaluation of the FLUXCOM approach. *Biogeosciences* **17**, 1343–1365 (2020).
16. J. Joiner *et al.*, Estimation of terrestrial global gross primary production (GPP) with satellite data-driven models and eddy covariance flux data. *Remote Sens.* **10**, 1346 (2018).
17. S. W. Running, M. Zhao, User's Guide: Daily GPP and annual NPP (MOD17A2/A3) products NASA Earth Observing System MODIS land algorithm. https://www.ntsg.umt.edu/files/modis/MOD17UsersGuide2015_v3.pdf. Accessed 1 May 2019.
18. P. Mahadevan *et al.*, A satellite-based biosphere parameterization for net ecosystem CO_2 exchange: Vegetation Photosynthesis and Respiration Model (VPRM). *Global Biogeochem. Cycles* **22**, GB2005 (2008).
19. D. N. Huntzinger *et al.*, North American Carbon Program (NACP) regional interim synthesis: Terrestrial biospheric model intercomparison. *Ecol. Modell.* **232**, 144–157 (2012).
20. K. Schaefer *et al.*, Combined simple biosphere/Carnegie-Ames-Stanford approach terrestrial carbon cycle model. *J. Geophys. Res. Biogeosci.* **113**, g03034 (2008).
21. P. J. Sellers, Y. Mintz, Y. C. Sud, A. Dalcher, A simple biosphere model (SIB) for use within general circulation models. *J. Atmos. Sci.* **43**, 505–531 (1986).
22. A. Anav *et al.*, Spatiotemporal patterns of terrestrial gross primary production: A review. *Rev. Geophys.* **53**, 785–818 (2015).
23. T. W. Hilton *et al.*, Peak growing season gross uptake of carbon in North America is largest in the Midwest USA. *Nat. Clim. Chang.* **7**, 450–454 (2017).
24. J. B. Fisher *et al.*, Carbon cycle uncertainty in the Alaskan Arctic. *Biogeosciences* **11**, 4271–4288 (2014).
25. Y. Sun *et al.*, OCO-2 advances photosynthesis observation from space via solar-induced chlorophyll fluorescence. *Science* **358**, eaam5747 (2017).
26. G. Badgley, C. B. Field, J. A. Berry, Canopy near-infrared reflectance and terrestrial photosynthesis. *Sci. Adv.* **3**, e1602244 (2017).
27. C. Frankenberg *et al.*, New global observations of the terrestrial carbon cycle from GOSAT: Patterns of plant fluorescence with gross primary productivity. *Geophys. Res. Lett.* **38**, L17706 (2011).
28. N. C. Parazoo *et al.*, Towards a harmonized long-term spaceborne record of far-red solar-induced fluorescence. *J. Geophys. Res. Biogeosci.* **124**, 2518–2539 (2019).
29. L. Guanter *et al.*, Retrieval and global assessment of terrestrial chlorophyll fluorescence from GOSAT space measurements. *Remote Sens. Environ.* **121**, 236–251 (2012).
30. G. Badgley, L. D. L. Anderegg, J. A. Berry, C. B. Field, Terrestrial gross primary production: Using NIR_V to scale from site to globe. *Glob. Change Biol.* **25**, 3731–3740 (2019).
31. A. Zumkehr *et al.*, Global gridded anthropogenic emissions inventory of carbonyl sulfide. *Atmos. Environ.* **183**, 11–19 (2018).
32. J. E. Campbell *et al.*, Large historical growth in global terrestrial gross primary production. *Nature* **544**, 84–87 (2017).
33. J. E. Campbell *et al.*, Photosynthetic control of atmospheric carbonyl sulfide during the growing season. *Science* **322**, 1085–1088 (2008).
34. S. A. Montzka *et al.*, On the global distribution, seasonality, and budget of atmospheric carbonyl sulfide (COS) and some similarities to CO_2. *J. Geophys. Res. D Atmospheres* **112**, D09302 (2007).
35. J. Berry *et al.*, A coupled model of the global cycles of carbonyl sulfide and CO_2: A possible new window on the carbon cycle. *J. Geophys. Res. Biogeosci.* **118**, 842–852 (2013).
36. A. J.KettleU.KuhnM.von HobeJ.KesselmeierM. O.Andreae, Global budget of atmospheric carbonyl sulfide: Temporal and spatial variations of the dominant sources and sinks. *J. Geophys. Res. Atmos.* **107**, ACH 25-21–ACH 25-16 (2002).
37. M. E. Whelan *et al.*, Reviews and syntheses: Carbonyl sulfide as a multi-scale tracer for carbon and water cycles. *Biogeosciences* **15**, 3625–3657 (2018).
38. M. E. Whelan *et al.*, Carbonyl sulfide exchange in soils for better estimates of ecosystem carbon uptake. *Atmos. Chem. Phys.* **16**, 3711–3726 (2016).
39. M. E. Whelan, D.-H. Min, R. C. Rhew, Salt marsh vegetation as a carbonyl sulfide (COS) source to the atmosphere. *Atmos. Environ.* **73**, 131–137 (2013).
40. K. Maseyk *et al.*, Sources and sinks of carbonyl sulfide in an agricultural field in the Southern Great Plains. *Proc. Natl. Acad. Sci. U.S.A.* **111**, 9064–9069 (2014).
41. L. M. J. Kooijmans *et al.*, Influences of light and humidity on carbonyl sulfide-based estimates of photosynthesis. *Proc. Natl. Acad. Sci. U.S.A.* **116**, 2470–2475 (2019).
42. R. Commane *et al.*, Seasonal fluxes of carbonyl sulfide in a midlatitude forest. *Proc. Natl. Acad. Sci. U.S.A.* **112**, 14162–14167 (2015).
43. L. M. J. Kooijmans *et al.*, Canopy uptake dominates nighttime carbonyl sulfide fluxes in a boreal forest. *Atmos. Chem. Phys.* **17**, 11453–11465 (2017).
44. Y. Zhang, J. Joiner, S. H. Alemohammad, S. Zhou, P. Gentine, A global spatially contiguous solar-induced fluorescence (CSIF) dataset using neural networks. *Biogeosciences* **15**, 5779–5800 (2018).
45. K. Huang *et al.*, Enhanced peak growth of global vegetation and its key mechanisms. *Nat. Ecol. Evol.* **2**, 1897–1905 (2018).
46. X. Lin *et al.*, Siberian and temperate ecosystems shape Northern Hemisphere atmospheric CO2 seasonal amplification. *Proc. Natl. Acad. Sci. U.S.A.* **117**, 21079–21087 (2020).
47. L. Hu *et al.*, Enhanced North American carbon uptake associated with El Niño. *Sci. Adv.* **5**, eaaw0076 (2019).
48. S. Kim, ppcor: An R package for a fast calculation to semi-partial correlation coefficients. *Commun. Stat. Appl. Methods* **22**, 665–674 (2015).
49. R. R. Nemani *et al.*, Climate-driven increases in global terrestrial net primary production from 1982 to 1999. *Science* **300**, 1560–1563 (2003).
50. J. Liu, P. O. Wennberg, N. C. Parazoo, Y. Yin, C. Frankenberg, Observational constraints on the response of high-latitude northern forests to warming. *AGU Adv.* **1**, e2020AV000228 (2020).
51. R. J. Norby, J. M. Warren, C. M. Iversen, B. E. Medlyn, R. E. McMurtrie, CO_2 enhancement of forest productivity constrained by limited nitrogen availability. *Proc. Natl. Acad. Sci. U.S.A.* **107**, 19368–19373 (2010).
52. A. Arneth *et al.*, Terrestrial biogeochemical feedbacks in the climate system. *Nat. Geosci.* **3**, 525 (2010).
53. R. J. Donohue, M. L. Roderick, T. R. McVicar, G. D. Farquhar, Impact of CO_2 fertilization on maximum foliage cover across the globe's warm, arid environments. *Geophys. Res. Lett.* **40**, 3031–3035 (2013).
54. I. H. Myers-Smith *et al.*, Shrub expansion in tundra ecosystems: Dynamics, impacts and research priorities. *Environ. Res. Lett.* **6**, 045509 (2011).
55. Z. A. Mekonnen, W. J. Riley, J. T. Randerson, R. F. Grant, B. M. Rogers, Expansion of high-latitude deciduous forests driven by interactions between climate warming and fire. *Nat. Plants* **5**, 952–958 (2019).
56. C. Sweeney *et al.*, Seasonal climatology of CO2 across North America from aircraft measurements in the NOAA/ESRL Global Greenhouse Gas Reference Network. *J. Geophys. Res. Atmos.* **120**, 5155–5190 (2015).
57. A. E. Andrews *et al.*, CO_2, CO, and CH_4 measurements from tall towers in the NOAA Earth System Research Laboratory's Global Greenhouse Gas Reference Network: Instrumentation, uncertainty analysis, and recommendations for future high-accuracy greenhouse gas monitoring efforts. *Atmos. Meas. Tech.* **7**, 647–687 (2014).
58. T. Nehrkorn *et al.*, Coupled weather research and forecasting–stochastic time-inverted Lagrangian transport (WRF–STILT) model. *Meteorol. Atmos. Phys.* **107**, 51–64 (2010).
59. J. Ma *et al.*, Inverse modelling of carbonyl sulfide: Implementation, evaluation and implications for the global budget. *Atmos. Chem. Phys. Discuss.* **2020**, 1–39 (2020).

60. G. R. van der Werf *et al*., Global fire emissions estimates during 1997–2016. *Earth Syst. Sci. Data* **9**, 697–720 (2017).
61. M. O. Andreae, Emission of trace gases and aerosols from biomass burning—An updated assessment. *Atmos. Chem. Phys.* **19**, 8523–8546 (2019).
62. P. Suntharalingam, A. J. Kettle, S. M. Montzka, D. J. Jacob, Global 3-D model analysis of the seasonal cycle of atmospheric carbonyl sulfide: Implications for terrestrial vegetation uptake. *Geophys. Res. Lett.* **35**, L19801 (2008).
63. K. Haynes, I. Baker, S. Denning, *The Simple Biosphere Model Version 4.2: SiB4* (Colorado State University, Fort Collins, CO, 2020).
64. A. M. Michalak, L. Bruhwiler, P. P. Tans, A geostatistical approach to surface flux estimation of atmospheric trace gases. *J. Geophys. Res. D Atmospheres* **109**, D14109 (2004).
65. S. M. Miller *et al*., Anthropogenic emissions of methane in the United States. *Proc. Natl. Acad. Sci. U.S.A.* **110**, 20018–20022 (2013).
66. L. Hu *et al*., Continued emissions of carbon tetrachloride from the United States nearly two decades after its phaseout for dispersive uses. *Proc. Natl. Acad. Sci. U.S.A.* **113**, 2880–2885 (2016).
67. L. Hu *et al*., Considerable contribution of the Montreal Protocol to declining greenhouse gas emissions from the United States. *Geophys. Res. Lett.* **44**, 8075–8083 (2017).
68. L. Hu *et al*., U.S. emissions of HFC-134a derived for 2008–2012 from an extensive flask-air sampling network. *J. Geophys. Res. Atmos.* **120**, 801–825 (2015).
69. K. A. Masarie, P. P. Tans, Extension and integration of atmospheric carbon dioxide data into a globally consistent measurement record. *J. Geophys. Res.* **100**, 11593–11610 (1995).
70. A. R. Jacobson *et al*., (2018) CarbonTracker CT2017 (http://carbontracker.noaa.gov). (Global Monitoring Laboratory, ESRL, NOAA).